ARTICLE

Check for updates

Pre-ceramic polymer-assisted nucleation and growth of copper sulfide nanoplates

Patricia A. Loughney [1], Kara L. Martin[2], Paul Cuillier[1], Edward B. Trigg[3,4,5], Nicholas D. Posey [3,4], Matthew B. Dickerson[3], Timothy L. Pruyn[3] & Vicky Doan-Nguyen [1✉]

Polymer-derived ceramics derived from pre-ceramic polymers (PCPs), have access to several form factors and are highly tunable systems. Tunability can be further expanded with the incorporation of functional nanoparticle fillers throughout the matrix for advanced nano-composite polymer-derived ceramic development. However, capping ligands used in nano-particle syntheses mix unfavorably with PCPs, giving aggregated filler material and diminished properties. To control dispersion, secondary nanoparticle processing is performed by adhering PCP-miscible caps to the surface after synthesis. This often sacrifices size control established for small nanoparticles (<10 nm). Herein, we successfully eliminate the need for extra nanoparticle processing through the development of a one-pot, copper sulfide synthesis in which a PCP assists the stable formation of nanoparticles and serves as the final graft molecule. We monitor the success of this methodology and the PCP's role in the reaction through several characterization methods probing both the nanoparticle core and polymer graft.

---

[1] Materials Science and Engineering, The Ohio State University, Columbus, OH 43210, USA. [2] Aerospace Systems Directorate, Air Force Research Laboratory, Wright-Patterson AFB, OH 45433, USA. [3] Materials and Manufacturing Directorate, Air Force Research Laboratory, Wright-Patterson AFB, OH 45433, USA. [4] UES, Inc, Dayton, OH 45432, USA. [5]Present address: Cambium Biomaterials, Inc., Mojave, CA 93501, USA. ✉email: vicky.d.trigg@aero.org

Polymer-derived ceramics (PDC) are a subset of ceramics that have been investigated in the past few decades because of their processability and increased tailorability with the inclusion of functional nanoparticle fillers[1–10]. Access to canonical polymer processing methodologies provides the industrial advantage, enabling further streamlined manufacturing capabilities such as fiber spinning, blowing, injection molding, warm pressing, and 3D printing[11]. PDC tailorability starts with their derivation from pre-ceramic polymers (PCP), which gives option to tune backbone and sidechain groups beyond functional starting chains[12]. Tailorability is taken even further with inclusion of nanoparticle filler, which improves PDC structural integrity through densification[1,5] but also provides a pathway for PDCs embedded with functional nanoparticle properties[2,13–17].

Optimizing filler structural support and property percolation requires control of dispersion of nanoparticles within PCPs. This is challenging[18] and is made more difficult by the poor miscibility between conventional nanoparticle capping ligands and PCP materials. Modifying nanoparticle surfaces with polymer-grafts promotes enhanced dispersion into similar polymer matrices[18–20]. Though promising for better nanofiller dispersion into PCP matrices, only a few studies have applied this grafting technique to advanced PDC development[21,22]. Ligand exchange and graft methodologies in the grafted nanoparticle field have been well-developed for polymers. However, size control is sacrificed, especially for reactive or small (<10 nm) particles[19]. We address the gap for developing a one-step, size-controlled synthesis and graft methodology for PCP-dispersible nanoparticle filler material for eventual processing into advanced nanocomposite PDCs.

Nanostructure synthetic strategies are well-developed for tight size and morphological control through bottom-up thermolysis to harness LaMer nucleation and growth kinetics[23,24]. In the presence of a metal salt, these methods use a reducing agent to aid in monomer saturation prior to nucleation, and a capping ligand to provide surface protection or tune growth kinetics[25]. Common capping ligands are long, hydrocarbon chains with active end groups such as amines[26,27], carboxylic acid[27,28], thiols[29–31], or diols[32,33] that adhere to the hydrophilic surface of the nanoparticle via chemi- or physisorption. They have been extended to include polymers, such as polyvinylpyrrolidone which has three possible functional groups for capping[34–36]. Despite the diversity of molecules explored, absent in both nanoparticle and grafted nanoparticle literature are the use of PCPs equipped with functional end groups for nanoparticle capping during synthesis.

A candidate for the PCP in such a synthesis is poly(pyridylmercaptopropyl)methylsiloxane (PyMPS), a polysiloxane with thioether sidechains containing a pyridine moiety[22]. This pyridine moiety was designed as a capping site during

nanoparticle synthesis, similar to what has been reported for polyvinylpyrrolidone. The linker thioether on the PyMPS sidechain was also designed to be a reactant with transition metals for chalcogenide production. This approach leveraging both nitrogen and sulfur atoms within the polymer is expected to form PDC nanocomposites containing transition metal chalcogenides with a variety of interesting properties and applications[37–40]. We explored the synergistic chemistry of this PCP herein.

This study reports a one-pot reaction scheme that eliminates the need for a two-step graft reaction to form a PCP-dispersible, grafted nanoparticle in a pre-ceramic polymer-assisted nucleation and growth (PPANG) method. Here, we produce copper(I) sulfide (Cu_2S) by using PyMPS not only as a capping ligand, but also as a reactant, reducing agent, and possible shape-directing agent during thermolysis. Particles synthesized herein demonstrate size control and show potential to be easily dispersed in similar PCP matrices prior to PDC processing.

Results and discussion

Core nanoparticle characterization. PPANG-formed nanoparticles were produced following a bottom-up, conventional thermolysis methodology where all or most of the traditional capping ligand was replaced with a PCP, PyMPS (Fig. 1). Reported herein are the results of an intensive look into PPANG as a viable methodology in the case of Cu_2S and PyMPS chemistries.

Upon substituting oleylamine with PyMPS, a $P2_1/c$ (ICSD CIF #100333) Cu_2S core is formed as confirmed by synchrotron X-ray diffraction (XRD) (Fig. 2a). The formation of a sulfide species upon replacing oleylamine with PyMPS confirms PyMPS as a sulfur-donating reactant despite sulfur's nonterminal location in the sidechain.

Average nanoparticle size is calculated via Rietveld refinement. The nanoplate size range was 3.4–9.7 nm depending on ligand loading (Fig. 2a). Average lateral plate dimension decreases with decreasing oleylamine concentration. The size range achieved with PPANG of Cu_2S nanoparticles is smaller than the estimates for oleylamine-formed copper nanoparticles (8–16 nm) from which our PPANG methodology is based (Supplementary Fig. 1).

We apply pair distribution function (PDF) analysis to characterize the local structure of the Cu_2S nanoparticles and their capping ligands. PDF analysis considers both Bragg scattering from nanocrystalline Cu_2S and diffuse scattering from the polymers with only short-range order. This reciprocal-space total scattering pattern is Fourier transformed to a real-space pair distribution function, G(r), representing a histogram of interatomic distances in the sample. Figure 2b shows the <5 Å range of the PDF for the as-received liquid capping ligands and three Cu_2S samples synthesized with varying PyMPS:oleylamine ratios. Peaks
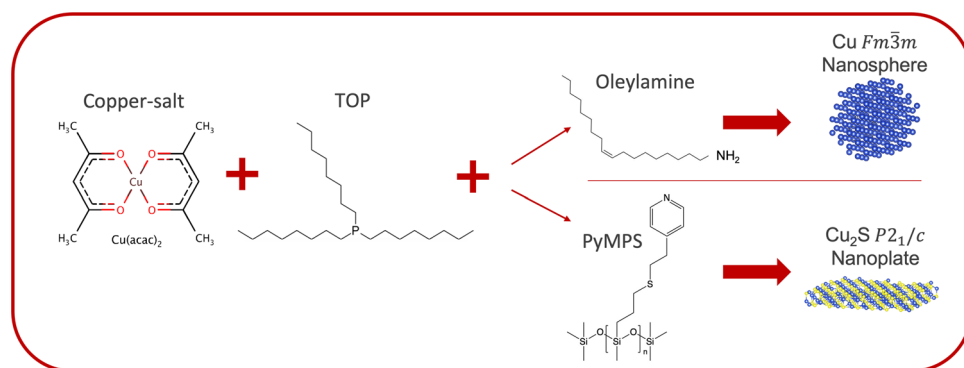
Fig. 1 PPANG vs conventional thermolysis approaches. Preceramic polymer assisted nucleation and growth (PPANG) uses poly(pyridylmercaptopropyl) methylsiloxane (PyMPS) to produce distinctive nanostructures not accessible via conventional thermolysis.
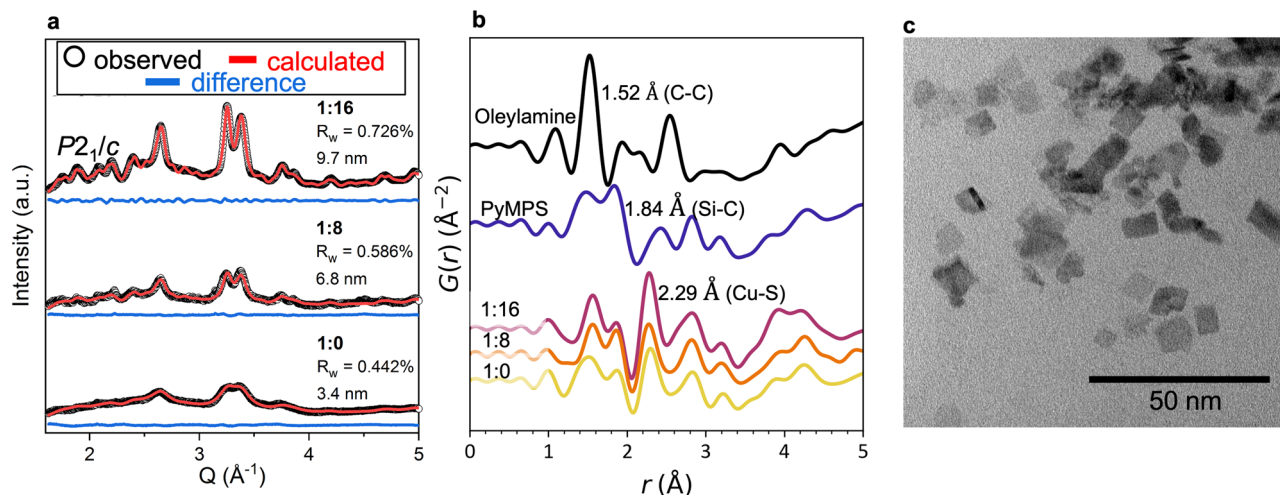
Fig. 2 XRD and TEM of Cu₂S nanoparticles. XRD (**a**) and Rietveld refinement (Cu₂S P2₁/c ICSD #100333) of particles formed with three unique ligand ratios show a decrease in fitted size with decreasing oleylamine concentration (PyMPS:oleylamine 1:y, y = 16, 8, 0). PDF over these changing ligand ratios confirms particle-PyMPS polymer interactions at low-r (**b**). TEM reveals a platelike morphology for the particles formed with a 1:16 ligand ratio (**c**).

with $r < 2.3$ Å (Cu–S bond) are attributed to the capping ligands. Bulk oleylamine shows a single intense peak at 1.52 Å from sp^3 C–C chains[41]. Si–O and Si–C bonds in PyMPS backbone correspond to peaks at ~1.5 Å and ~1.8 Å[42]. The sidechains contribute additional intensity to the 1.8 Å peak with C–S bonds (1.83 Å) and asymmetry in the 1.5 Å peak from C–C bonds in the thiol chain (1.52 Å) and the pyridine group (1.38 Å). All Cu₂S samples show a pair of peaks resembling PyMPS, indicating PyMPS's function as the primary capping ligand even at high concentrations of oleylamine. However, compared to bulk PyMPS, the relative intensities of the 1.5 and 1.8 Å peaks are reversed in the Cu₂S samples. At 1:16 and 1:8 PyMPS to oleylamine ratios, this may be explained by a combination of oleylamine and PyMPS capping ligands, but this feature is also observed without any oleylamine (1:0). This suggests the composition of the coordinating ligands differs from pristine PyMPS, which is to be expected if the bridging thiol from the sidechain is incorporated in the nanoparticle core. This sample also has a 1.4 Å shoulder present in bulk PyMPS PDF, which suggests pyridine groups are present in the absence of oleylamine. However, Cu-N bond lengths in metal-organic complexes are typically 2.0–2.1 Å, which is distinctly a minimum in the PDF[41]. Thus, pyridine coordination at the nanoparticle surface is likely less significant than coordination through Cu–S (2.2–2.3 Å) interactions.

Transmission electron microscopy (TEM) images reveal PPANG-formed small particles of low contrast exhibiting a rectangular plate-like morphology for PPANG-formed nanoparticles with anisotropy higher than expected for the monoclinic Cu₂S crystal lattice (Fig. 2c). This polymer-induced, forced anisotropy in the PPANG-formed Cu₂S nanoplates is different behavior than what is occurring in the spherical, oleylamine-formed copper nanoparticles (Supplementary Fig. 1b). With oleylamine, strong and equal binding to all facets maintains the expected isotropic growth of the cubic, copper lattice. PyMPS must be binding by a different mechanism to provide preferential growth in certain facets for Cu₂S. Finally, the rectangular plate shape is a distinctive Cu₂S nanostructure, as the majority of reported syntheses form nanorods[43] or nanodisks that are either circular[44], elongated[45], or hexagonal[33]. In addition to sulfur donation, PyMPS must also direct shape to form a morphology of higher anisotropy than expected for the characterized lattice.

PyMPS characterization. Fourier transform infrared (FTIR) spectroscopy confirms that the PyMPS ligand remains bound to nanoparticle cores at every ligand ratio (Fig. 3, Supplementary Fig. 2). This is based on PyMPS characteristic vibrational modes which are present in the neat polymer and all nanoparticle spectra: 1300–1600 cm⁻¹ (C–N), 1250 cm⁻¹ (Si–CH₃), 1020 cm⁻¹ (Si–O–Si), 950 cm⁻¹ (Si–CH), and 820 cm⁻¹ (Si–C), which are each retained in the nanostructured Cu₂S samples.

Unbound pyridine is present in all products and corresponds to strong peaks at 1600 cm⁻¹ and 1415 cm⁻¹ (red arrows, Fig. 3b)[22]. Coordinated pyridine FTIR signatures for PyMPS:oleylamine 3:16 molar equivalents (highest PyMPS loading) appear as small shoulders blue-shifted from the uncoordinated peaks at 1640 and 1455 cm⁻¹ (blue dashed arrows, Fig. 3b). In contrast, the coordinated pyridine FTIR signature is undetectable at lower PyMPS concentrations (Supplementary Fig. 2b). Thus, coordinated pyridine from PyMPS is a capping ligand concomitant with oleylamine; however, it is not the main capping ligand.

A strong peak at 727 cm⁻¹ (Fig. 3c) and a pronounced peak shoulder from the Si–O–Si vibration at 1020 cm⁻¹ are present in all nanoparticle FTIR spectra, but not the neat ligand spectra. The 727 cm⁻¹ vibration is not attributable to oleylamine since the characteristic frequency remains in the nanoparticle sample in absence of oleylamine (1:0 PyMPS:oleylamine, Supplementary Fig. 2c). Thus, the peak at 727 cm⁻¹ and shoulder off of Si-O-Si at 1020 cm⁻¹ are attributed to Cu–S vibrations for Cu₂S[46].

Role of PyMPS in PPANG. In-situ small-angle X-ray scattering (SAXS) during nanoparticle growth (Fig. 4a–c) captures the assistive role of PyMPS in nucleation and growth at varied ligand ratios. Similar to conventional thermolysis, PyMPS assists in stabilization of nanoparticle nucleation to the critical radius, thus enabling growth even in the reaction devoid of oleylamine (Fig. 4c)[26]. Nanoplate dimension (radius of gyration, R_g) was calculated from SAXS fits in the Guinier and Porod regions (Fig. 4d–f) and compared for each ligand ratio (Fig. 4g). Details about fitting parameters and normalized residuals for each model can be found in Supplementary Fig. 3. Based on the fit sizes and the TEM of these nanoplates (Fig. 2c), this dimension is an average radius from the largest, stabilized facet of the plates. Thickness and plate aspect ratio are not able to be quantified with high certainty due to low-Q data limitations.
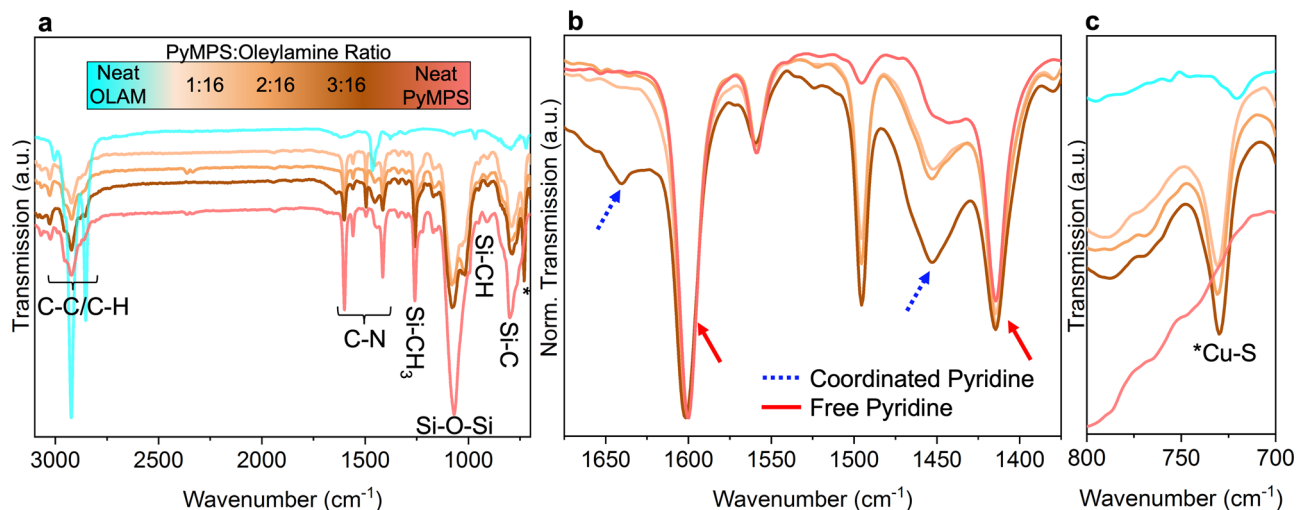
Fig. 3 FTIR of PPANG-formed Cu₂S nanoparticles. Spectra were collected for nanoparticles with increasing PyMPS loading compared to neat oleylamine and PyMPS. In each particle FTIR spectra, we see that PyMPS remains largely intact across all samples (**a**). A closer look at the pyridine region shows diminishing free pyridine with increasing PyMPS, and the eventual appearance of coordinated pyridine at the highest loading of PyMPS (**b**). Zooming in at about 727 cm⁻¹ shows a Cu–S bond vibration for each sample, likely from the nanoparticle core (**c**).
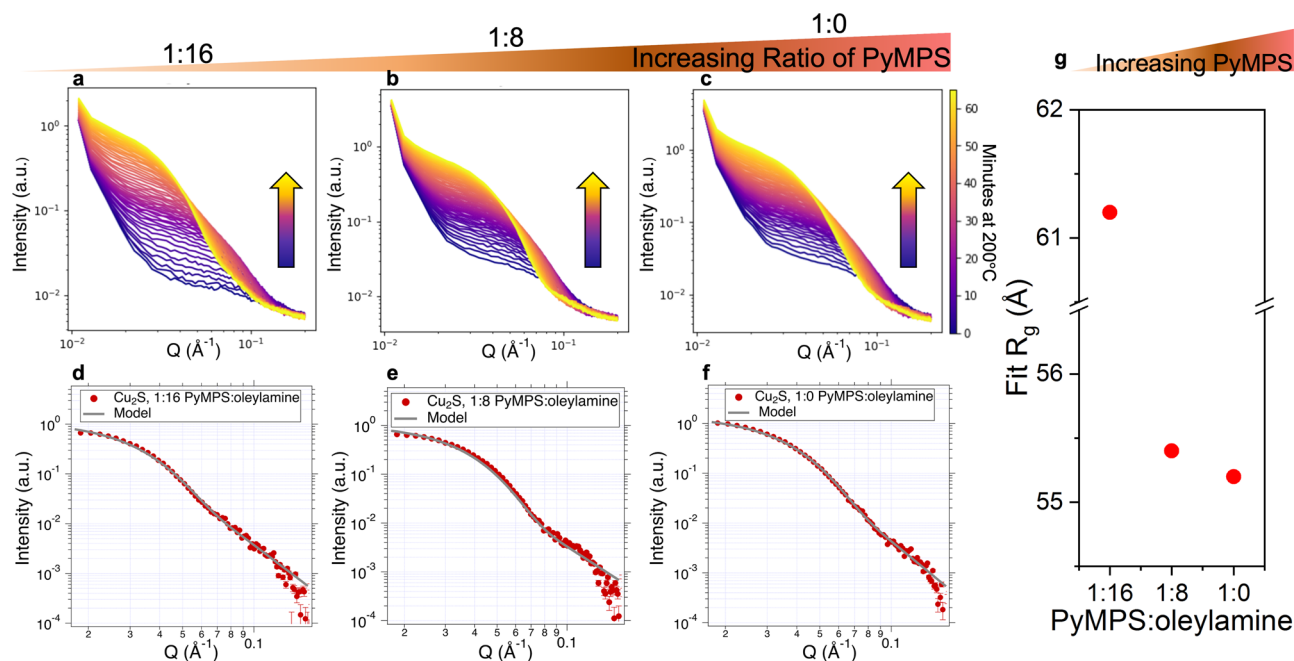

Fig. 4 In situ SAXS during PPANG Cu₂S growth. This is performed over increasing PyMPS ratio, where a SAXS scan was acquired every minute during the final temperature hold of 200 °C (**a–c**). The growth of a Guinier knee (yellow arrow) at low-q indicates a nanoparticle formation. Final scans from each experiment were background subtracted and fit (**d–f**) to understand the changing radius of gyration with changing ligand loadings. Overall, there is a decreased average radius of gyration from the main scatterer population with increasing ratio of PyMPS:oleylamine (**g**).

With increasing PyMPS:oleylamine ratio, R_g decreases from 61 to 55 Å. The largest change in size is exhibited between ratios 1:16 and 1:8, which decreases at a rate of 0.725 Å per equivalent molar concentration decrease in oleylamine. Between 1:8 and 1:0 PyMPS:oleylamine molar ratios, the decrease is much less pronounced (0.02 Å per equivalent molar concentration). Because the functionalized PyMPS sidechain is within the repeating unit, PyMPS contributes a high concentration of functional groups to interact with the nanoparticles for ratios less than 1:16 PyMPS:oleylamine. At 1:8 and 1:0, the amount of PyMPS functional groups dominates. Ratios below the critical threshold of 1:16 produces nanostructures with similar dimensions.

TEM of particles formed with all three ligand ratios reveal that samples formed with any amount of oleylamine give a bimodal size distribution (Supplementary Fig. 4). However, the formation of larger particles is inhibited as the ratio of PyMPS increases. This is due to the higher degree of steric hindrance from PyMPS.

Nuclear magnetic resonance (NMR) spectroscopy of nanoparticle precursors before and after mixing reveal precursor activity in the early stages of the PPANG reaction when Cu²⁺ is reduced (Supplementary Fig. 5). Trioctylphosphine (TOP) and oleylamine exhibit minor peak shifts due to differences in solvent, thus, indicating a lack of interaction with copper salt upon initial mixing. Similarly, the PyMPS backbone (Si–CH₃, δ ≈ 0 ppm) and
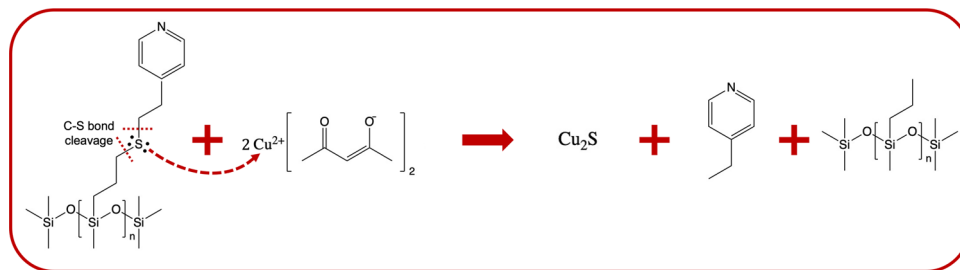
Fig. 5 Cu²⁺ reduction mechanism with PyMPS. PyMPS bond cleavage occurs during Cu(II) reduction to Cu(I), as confirmed by cross-correlative characterization.

Si–CH₂–CH₂–CH₂–S ($\delta \approx 0.5$ ppm -2 ppm) chain signals remain unchanged upon mixing in the precursor mixture. Significant shifts, however, are observed for the pyridinyl-sidechain in PyMPS post-mixing with precursors. Disappearance of two peaks that relate to S–CH₂–CH₂–py (between 2 ppm and 2.5 ppm, Supplementary Fig. 5a) indicate that ethyl pyridine is cleaved when the polymer is in the presence of the copper salt. This is possibly due to oxidative insertion of Cu between bridging sulfur and remaining sidechain (Fig. 5). Transition metal bond cleavage and insertion onto a C–S bond has been reported for several metals[47] including copper ions[48,49].

Cu₂S formation is from the reducing, S-donating capabilities of PyMPS in the PPANG reaction with ethyl pyridine as a possible byproduct in the PyMPS reduction of Cu(II) to Cu(I) (Fig. 5). Ethyl pyridine could either coordinate to the nanoparticle surface through the amine or remain free in the supernatant after nanoparticle flocculation. Such pyridine capping is corroborated by FTIR. Although it is below the limit of detection for NMR (Supplementary Fig. 6), liquid chromatography-mass spectrometry (LC-MS) confirms that ethyl pyridine (Supplementary Table 1) is also present in the supernatant post nanoparticle flocculation and centrifugation (Supplementary Fig. 7). This confirms ethyl pyridine cleavage from the polymer sidechain after Cu(II) reduction.

Proposed PyMPS graft mechanisms. Despite the Cu(II) reduction splitting the PyMPS side chain at the thiol, FTIR shows an intact polymer on the flocculated nanoparticle material post centrifugation, including the Si-O backbone. TEM-EDS of aggregated nanoparticles also reveal a mass of Si–O interaction surrounding the Cu₂S particle surfaces (Fig. S8). This infers that the backbone of PyMPS is remaining near the particle surfaces through exhaustive cleaning steps, likely acting as a capping ligand with a strong graft to the nanoparticle surface via chemisorption.

While previous FTIR suggests some pyridine capping from PyMPS, it is likely not the main capping mechanism due to the small size of nanoparticles and the small evidence of coordinated pyridine present in the FTIR spectrum. NMR and known literature suggest oxidative insertion of Cu(II) to cleave the ethyl pyridine, and LC-MS has reinforced that ethyl pyridine is left behind in solution. This seems to conflict with the intact nature of the polymer and its remaining association with the nanoparticles surfaces through cleaning steps. However, in the current methodology there is a stoichiometric excess of sulfur in the amount of PyMPS added to the reaction to sufficiently reduce Cu(II) to Cu(I) as it exists in Cu₂S. Therefore, some branches will not participate in Cu(II) reduction and never become cleaved. This leads to a variety of possible capping mechanisms from the PyMPS sidechain after Cu₂S formation (Fig. 6) or direct interaction between the backbone and surface metal sites in the nanoplate.

The plate morphology indicates facets along the direction perpendicular to the basal plane is sterically hindered. The polymer could cap such facets through the sidechain via either (pyridine) N–Cu (nanoparticle) coordination, (PyMPS sidechain) S–S (nanoparticle) coordination, (PyMPS sidechain) S–Cu (nanoparticle), or a combination of the three. Alternatively, O-interaction between the PyMPS backbone and surface Cu sites is also possible through lone pair donation and coordination, allowing the polymer to lay along the basal plane of the nanoplate. Faster growing facets are likely capped with lower molecular weight species such as decomposed oligomeric PyMPS or remaining ethyl pyridine after reduction.

Conclusion

Cu₂S nanoplates have been formed from a unique PyMPS pre-ceramic polymer-assisted nucleation and growth (PPANG) process. First, PyMPS acts as a reducing agent by successfully reducing Cu(II) to Cu(I) in the initial stage of the reaction through interactions with the thioether moiety in the polymer sidechain. Second, PyMPS dually acts as the sulfur source in the reaction. TEM revealed the formation of highly anisotropic nanoplates, alluding to facetted stabilization originating from PyMPS acting as a capping ligand. SAXS and XRD have confirm size control via varying PyMPS:oleylamine concentration with the smallest R_g stabilized by only PyMPS. Unreacted polymer sidechains of PyMPS are, therefore, chemisorbed to the nanoplates. This interaction between PyMPS and nanoparticle core is also supported in the low-r portion of the PDF. FTIR indicates pyridine coordination at high PyMPS loadings. This approach leverages multiple aspects of a polymer's chemical structure to create nanocomposites and opens future opportunities to use dual-role preceramic polymers to both synthesize and shape the resulting nanomaterial. In a one-pot approach, we have successfully controlled the formation of a PCP-grafted nanoparticle that shows promise for enhanced dispersion into PCPs, for eventual processing into advanced PDCs with functional properties.

Methods

Cu₂S materials. Copper(II) acetylacetonate, benzyl ether, hexane (extra dry, 96%), toluene (certified ACS), were each purchased from Fisher Scientific for use in the PPANG synthesis or processing. Trioctylphosphine (97%), oleylamine (technical grade, 70%), and 1-octadecene (technical grade, 90%) were each purchased from Sigma Aldrich for use in the PPANG synthesis. PyMPS was synthesized following previously reported methodology[22].

Cu₂S synthesis. Copper(II) acetylacetonate (0.15 mmol), oleylamine, PyMPS, and 7 mL 1-octadecene (or benzyl ether) were added to a three-neck flask, mixed, and purged with argon via Schlenk line. PyMPS was added in a 1:0.25 Cu(acac)₂:PyMPS molar ratio and oleylamine was added in a 1:4 Cu(acac)₂:oleylamine molar ratio, giving a 1:16 molar ligand ratio of PyMPS:oleylamine. This ligand loading ratio was varied between different experiments to include PyMPS:oleylamine ratios of 1:y ($y = 16, 8, 0$) and x:16 ($x = 1, 2, 3$). Once the mixture was purged, 0.462 mL of trioctylphosphine (TOP) was injected into the inert reaction and mixed. While mixing under argon, the reaction was heated to 80 °C at ≈°C/min and held for 15 min. Following the first heated hold, the reaction mixture was taken to its final
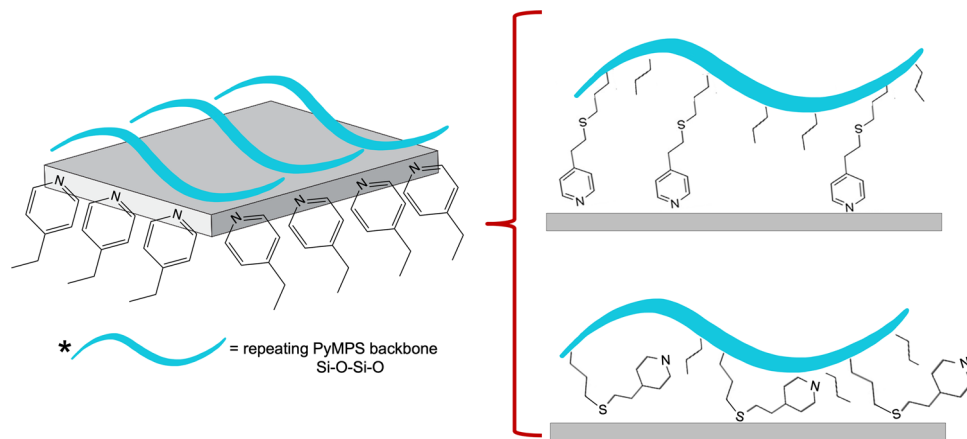
Fig. 6 Possible Cu₂S@PyMPS capping mechanisms. Nanoparticle-PCP capping could come from the PyMPS sidechain after Cu^{2+} reduction to Cu_2S, nucleation, and growth of Cu_2S nanoplates. We hypothesize that the PyMPS backbone is linked to the stabilized facet experiencing the least growth, as the backbone would provide steric hindrance due to its bulkiness (left). These could be linked via remaining un-cleaved PyMPS branches interacting with either the cation or anion of the nanoparticle through the amine on pyridine or the thioether on PyMPS (right). Lower molecular weight species (such as ethyl pyridine, or oligomers of PyMPS) could be interacting with the growth facets, allowing easier atomic addition than faces interacting with the PyMPS backbone (left).

reaction temperature of 200 °C at ~6 °C/min. The reaction was held at this temperature for 1 h before removing the heating source and allowing the flask to cool back to room temperature, all while remaining under argon. Particles were flocculated using toluene and hexane (as solvent and antisolvent, respectively) and centrifugation at 8000 RPM (7441 × *g* RCF) for 5 min. The supernatant was decanted, and the flocculated solid was redispersed and centrifuged two more times to clean the particle surface thoroughly. Finally, cleaned particles were dispersed in toluene for storage.

Characterization methods. Cu₂S nanoparticle cores were characterized with high energy X-ray scattering and pair distribution functions (PDF), transmission electron microscopy (TEM), and in situ small-angle X-ray scattering (SAXS). Polymer capping/grafting corona and linkage was characterized using Fourier transform infrared spectroscopy (FTIR). The role of PyMPS in the PPANG synthesis was examined using nuclear magnetic resonance spectroscopy (NMR) and liquid chromatography-mass spectroscopy (LC-MS) in combination of all techniques mentioned above.

High energy X-ray scattering data for PDF was collected on samples at the Advanced Photon Source at Argonne National Laboratory beamline 11-ID-B ($\lambda = 0.2115$ Å) under GUP-74463. Calibration and Rietveld refinements were performed in GSAS-II[50]. A Ni standard was used to calibrate the sample-detector distances for X-ray diffraction (XRD) (700 mm) and PDF (200 mm) measurements and fit instrumental peak broadening parameters. The $S(Q)$ measured for PDF analysis was transformed to the reduced pair distribution function (Eq. 1)[51] using PDFgetX3[52,53]. The scale of the background scattering of the Kapton sample container was fixed, and Q_{max} and r_{poly} were set to values of 21.5 and 1.16 Å, respectively, to minimize Fourier transform termination ripples. All fits were performed to crystallographic information files gathered from the International Crystal Structure Database (ICSD) and are referenced throughout.

$$G(r) = \frac{2}{\pi} \int_{Q_{min}}^{Q_{max}} Q[S(Q) - 1]\sin(Qr)dQ \qquad (1)$$

Conventional TEM images were collected using an FEI Tecnai G2-30 at 300 kV equipped with a 4k CETA camera. STEM-EDS images were collected using an FEI Tecnai F20 TEM at 200 kV in nanoprobe mode. STEM images were acquired with a HAADF detector and elemental characterization was performed using large area EDAX SDD X-ray detector. TEM and STEM-EDS samples were prepped after the three centrifugation steps reported in the Cu₂S synthesis, followed by dilution in toluene and 5 additional minutes of centrifugation. Diluted samples were drop casted onto lacey carbon support film TEM grids (Cu, 400 mesh, 100 micron) for imaging.

SAXS patterns were collected using a XENOCS Xeuss 3.0 instrument equipped with a Pilatus3 300k detector. In-situ SAXS scans were taken on precursor mixtures of various ligand loading in a Linkam heated capillary holder. Precursor-loaded capillaries were heated following the same heating profile reported in the Cu₂S synthesis while SAXS scans were taken every minute at the final reaction temperature of 200 °C. Integration of all scans were performed using pyFAI[54] and fitting of each final scan was performed using the Unified Fit model[55,56] in Igor IRENA[57–60].

FTIR spectra were gathered using a Thermo Fisher Nicolet 6700 while in transmission mode. Each spectrum was scanned from 700–4000 cm^{-1} to capture both the full range of the polymeric signatures and particle core metal-sulfide vibrations.

NMR, LC-MS, Lab XRD, and X-ray fitting procedures and experimental information can be found in the Supporting Information.

References
1. Colombo, P., Mera, G., Riedel, R. & Sorarù, G. D. Polymer-derived ceramics: 40 years of research and innovation in advanced ceramics. *J. Am. Ceram. Soc.* **93**, 1805–1837 (2010).
2. Bernardo, E., Fiocco, L., Parcianello, G., Storti, E. & Colombo, P. Advanced ceramics from preceramic polymers modified at the nano-scale: a review. *Materials* **7**, 1927–1956 (2014).
3. Stabler, C., Ionescu, E., Graczyk-Zajac, M., Gonzalo-Juan, I. & Riedel, R. Silicon oxycarbide glasses and glass-ceramics: "all-rounder" materials for advanced structural and functional applications. *J. Am. Ceram. Soc.* **101**, 4817–4856 (2018).
4. Lu, K. & Erb, D. Polymer derived silicon oxycarbide-based coatings. *Int. Mater. Rev.* **63**, 139–161 (2018).
5. Barroso, G., Li, Q., Bordia, R. K. & Motz, G. Polymeric and ceramic silicon-based coatings-a review. *J. Mater. Chem. A* **7**, 1936–1963 (2019).
6. Xia, A., Yin, J., Liu, X. & Huang, Z. Polymer-derived Si-based ceramics: recent developments and perspectives. *Crystals* **10**, 1–19. (2020).
7. Ren, Z., Mujib, S., Bin & Singh, G. High-temperature properties and applications of Si-based polymer-derived ceramics: a review. *Materials* **14**, 614 (2021).
8. Sujith, R., Jothi, S., Zimmermann, A., Aldinger, F. & Kumar, R. Mechanical behaviour of polymer derived ceramics – a review. *Int. Mater. Rev.* **66**, 426–449 (2021).
9. Yang, N. & Lu, K. Porous and ultrahigh surface area SiOC ceramics based on perhydropolysilazane and polysiloxane. *Microporous Mesoporous Mater.* **306**, 110477 (2020).
10. Bréquel, H. et al. Systematic structural characterization of the high-temperature behavior of nearly stoichiometric silicon oxycarbide glasses. *Chem. Mater.* **16**, 2585–2598 (2004).
11. Wang, K. et al. Polymeric and ceramic silicon-based coatings-a review. *J. Am. Chem. Soc.* **7**, 1936–1963 (2021).
12. Key, T. S., Wilks, G. B. & Cinibulk, M. K. Effect of pendant groups on the mass yield and density of polycarbosilanes during pyrolysis. *J. Am. Ceram. Soc.* **105**, 2403–2410 (2022).
13. Wu, N., Wang, B. & Wang, Y. Enhanced mechanical properties of amorphous SiOC nanofibrous membrane through in situ embedding nanoparticles. *J. Am. Ceram. Soc.* **101**, 4763–4772 (2018).

14. Yousefi, M., Ghatee, M., Rezakazemi, M. & Ghaderi, S. H. The effects of adding nano-alumina filler on the properties of polymer-derived SiC coating. *Int. J. Appl. Ceram. Technol.* **18**, 2197–2206 (2021).

15. Yang, N., Gao, M., Li, J. & Lu, K. Nickel-containing magnetoceramics from water vapor-assisted pyrolysis of polysiloxane and nickel 2,4-pentanedionate. *J. Am. Ceram. Soc.* **103**, 145–157 (2020).

16. Hu, L. H. & Tsai, Y. T. Carbon fiber surface-modified by polymer derived ceramic incorporated with graphene to strengthen the mechanical and electrochemical properties of ceramic-carbon fiber composite. *Compos. Sci. Technol.* **221**, 109294 (2022).

17. Liu, H. & Webster, T. J. Mechanical properties of dispersed ceramic nanoparticles in polymer composites for orthopedic applications. *Int. J. Nanomed.* **5**, 299–313 (2010).

18. Krishnamoorti, R. Strategies for dispersing nanoparticles in polymers. *MRS Bull.* **32**, 341–347 (2007).

19. Chancellor, A. J., Seymour, B. T. & Zhao, B. Characterizing polymer-grafted nanoparticles: from basic defining parameters to behavior in solvents and self-assembled structures. *Anal. Chem.* **91**, 6391–6402 (2019).

20. Martin, T. B. et al. Wetting-dewetting and dispersion-aggregation transitions are distinct for polymer grafted nanoparticles in chemically dissimilar polymer matrix. *J. Am. Chem. Soc.* **137**, 10624–10631 (2015).

21. Martin, K. L., Street, D. P. & Dickerson, M. B. Polycarbosilane-grafted nanoparticles: free-flowing hairy nanoparticle liquids that convert to ceramic. *Chem. Mater.* **32**, 3990–4001 (2020).

22. Martin, K. L. et al. Bioinspired cross-linking of preceramic polymers via metal ion coordination bonding. *J. Eur. Ceram. Soc.* **41**, 6366–6376 (2021).

23. Bera, D., Qian, L., Tseng, T. K. & Holloway, P. H. Quantum dots and their multimodal applications: a review. *Materials* **3**, 2260–2345 (2010).

24. Pu, Y., Cai, F., Wang, D., Wang, J. X. & Chen, J. F. Colloidal synthesis of semiconductor quantum dots toward large-scale production: a review. *Ind. Eng. Chem. Res.* **57**, 1790–1802 (2018).

25. Loughney, P. A. & Doan-Nguyen, V. Synthesis of nanostructured materials for conversion of fuels. In *Clean Energy Materials*; vol. 1364, p. 189–206. ACS Symposium Series; American Chemical Society, 2020.

26. Mourdikoudis, S., Liz-marza, L. M., Liz-Marzán, L. M. & Liz-marza, L. M. Oleylamine in nanoparticle synthesis. *Chem. Mater.* **25**, 1465–1476 (2013).

27. Cui, F. et al. Synthesis of ultrathin copper nanowires using tris(trimethylsilyl) silane for high-performance and low-haze transparent conductors. *Nano Lett.* **15**, 7610–7615 (2015).

28. Fritzinger, B., Capek, R. K., Lambert, K., Martins, J. C. & Hens, Z. Utilizing self-exchange to address the binding of carboxylic acid ligands to CdSe quantum dots. *J. Am. Chem. Soc.* **132**, 10195–10201 (2010).

29. Medintz, I. L., Uyeda, H. T., Goldman, E. R. & Mattoussi, H. Quantum dot bioconjugates for imaging, labelling and sensing. *Nat. Mater.* **4**, 435–446 (2005).

30. Fafarman, A. T. et al. Thiocyanate-capped nanocrystal colloids: vibrational reporter of surface chemistry and solution-based route to enhanced coupling in nanocrystal solids. *J. Am. Chem. Soc.* **133**, 15753–15761 (2011).

31. Nag, A. et al. Metal-free inorganic ligands for colloidal nanocrystals: S2-, HS-, Se2-, HSe-, Te2-, HTe -, TeS32-, OH-, and NH 2- as surface ligands. *J. Am. Chem. Soc.* **133**, 10612–10620 (2011).

32. Rajh, T., Mićić, O. I. & Nozik, A. J. Synthesis and characterization of surface-modified colloidal CdTe quantum dots. *J. Phys. Chem.* **97**, 11999–12003 (1993).

33. Sigman, M. B. et al. Solventless synthesis of monodisperse Cu2S nanorods, nanodisks, and nanoplatelets. *J. Am. Chem. Soc.* **125**, 16050–16057 (2003).

34. Lo, S. H. Y., Wang, Y. Y. & Wan, C. C. Synthesis of PVP stabilized Cu/Pd nanoparticles with citrate complexing agent and its application as an activator for electroless copper deposition. *J. Colloid Interface Sci.* **310**, 190–195 (2007).

35. Xia, X., Zeng, J., Oetjen, L. K., Li, Q. & Xia, Y. Quantitative analysis of the role played by poly(vinylpyrrolidone) in seed-mediated growth of Ag nanocrystals. *J. Am. Chem. Soc.* **134**, 1793–1801 (2012).

36. Koczkur, K. M., Mourdikoudis, S., Polavarapu, L. & Skrabalak, S. E. Polyvinylpyrrolidone (PVP) in nanoparticle synthesis. *Dalt. Trans.* **44**, 17883–17905 (2015).

37. Giuffredi, G., Asset, T., Liu, Y., Atanassov, P. & Di Fonzo, F. Transition metal chalcogenides as a versatile and tunable platform for catalytic CO2 and N2 electroreduction. *ACS Mater. Au* **1**, 6–36 (2021).

38. Duay, J., Lambert, T. N., Kelly, M. & Pineda-Dominguez, I. Rechargeable solid-state copper sulfide cathodes for alkaline batteries: importance of the copper valence state. *J. Electrochem. Soc.* **166**, A687–A694. (2019).

39. Liu, Y., Liu, M. & Swihart, M. T. Plasmonic copper sulfide-based materials: a brief introduction to their synthesis, doping, alloying, and applications. *J. Phys. Chem. C* **121**, 13435–13447 (2017).

40. Mera, G., Gallei, M., Bernard, S. & Ionescu, E. Ceramic nanocomposites from tailor-made preceramic polymers. *Nanomaterials* **5**, 468–540 (2015).

41. Orpen, A. G., Brammer, L., Allen, F. H., Watson, D. G. & Taylor, R. Typical interatomic distances: organometallic compounds and coordination complexes of the d - and f -block metals. *Int. Tables Crystallogr.* **C**, 812–896 (2006).

42. Schitco, C. et al. Silicon oxycarbonitrides synthesized by ammonia-assisted thermolysis route from polymers: a total X-ray scattering, solid-state NMR, and TEM structural study. *J. Eur. Ceram. Soc.* **36**, 979–989 (2016).

43. Zheng, H. et al. Observation of transient structural-transformation dynamics in a Cu2S nanorod. *Science* **333**, 206–209 (2011).

44. Bryks, W., Wette, M., Velez, N., Hsu, S. W. & Tao, A. R. Supramolecular precursors for the synthesis of anisotropic Cu2S nanocrystals. *J. Am. Chem. Soc.* **136**, 6175–6178 (2014).

45. Zhuang, Z., Peng, Q., Zhang, B. & Li, Y. Controllable synthesis of Cu2S nanocrystals and their assembly into a superlattice. *J. Am. Chem. Soc.* **130**, 10482–10483 (2008).

46. SpectraBase Compound ID=AJKj5dtSvup SpectraBase Spectrum ID=KcsaoFh4MSp https://www.kcsao.com/spectrum/KcsaoFh4MSp.

47. Wang, L., He, W. & Yu, Z. Transition-metal mediated carbon–sulfur bond activation and transformations. *Chem. Soc. Rev.* **42**, 599–621 (2013).

48. Prabhakaran, R. et al. Copper ion mediated selective cleavage of C−S bond in ferrocenylthiose micarbazone forming mixed geometrical [(PPh3) Cu(μ-S) 2Cu(PPh3)2] having Cu2S2 core: toward a new avenue in copper−sulfur chemistry. *Inorg. Chem.* **51**, 3525–3532 (2012).

49. Fujisawa, K., Moro-Oka, Y. & Kitajima, N. Formation of a μ-H2:H2-disulfide dinuclear copper(II) complex by thermal decomposition of a thiolate complex via C-S bond cleavage. *J. Chem. Soc. Chem. Commun.* **379**, 623–624 (1994).

50. Toby, B. H. & Von Dreele, R. B. GSAS-II: the genesis of a modern open-source all purpose crystallography software package. *J. Appl. Crystallogr.* **46**, 544–549 (2013).

51. Peterson, P. F., Olds, D., McDonnell, M. T. & Page, K. Illustrated formalisms for total scattering data: a guide for new practitioners. *J. Appl. Crystallogr.* **54**, 317–332 (2021).

52. Juhás, P., Davis, T., Farrow, C. L. & Billinge, S. J. L. PDFgetX3: a rapid and highly automatable program for processing powder diffraction data into total scattering pair distribution functions. *J. Appl. Crystallogr.* **46**, 560–566 (2013).

53. Farrow, C. L. et al. PDFgui User Guide. *PDFGUI User Guid.* (2009).

54. Ashiotis, G. et al. The fast azimuthal integration Python library: PyFAI. *J. Appl. Crystallogr.* **48**, 510–519 (2015).

55. Ilavsky, J. & Jemian, P. R. *Irena SAS Modeling Macros Manual* **42**, 184 (2012).

56. Beaucage, G. Small-angle scattering from polymeric mass fractals of arbitrary mass-fractal dimension. *J. Appl. Crystallogr.* **29**, 134–146 (1996).

57. Ilavsky, J. & Jemian, P. R. Irena: tool suite for modeling and analysis of small-angle scattering. *J. Appl. Crystallogr.* **42**, 347–353 (2009).

58. Beaucage, G. Approximations leading to a unified exponential/power-law approach to small-angle scattering. *J. Appl. Crystallogr.* **28**, 717–728 (1995).

59. Nelson, A. Co-refinement of multiple-contrast neutron/X-ray reflectivity data using MOTOFIT. *J. Appl. Crystallogr.* **39**, 273–276 (2006).

60. Zhang, F. et al. Glassy carbon as an absolute intensity calibration standard for small-angle scattering. *Metall. Mater. Trans. A Phys. Metall. Mater. Sci.* **41**, 1151–1158 (2010).

Acknowledgements

Author contributions

P.A.L. performed all nanoparticle synthesis and processing, collected and analyzed the SAXS and microscopy data, collected the FTIR and synchrotron data, and wrote the text. K.L.M. provided the functionalized polysiloxane and aided in the operation and data analysis associated with NMR characterization. P.C. analyzed the synchrotron XRD and

Competing interests

The authors declare no competing interests.

Additional information

Supplementary information The online version contains supplementary material available at https://doi.org/10.1038/s43246-023-00380-5.

Correspondence and requests for materials should be addressed to Vicky Doan-Nguyen.

Peer review information *Communications Materials* thanks the anonymous reviewers for their contribution to the peer review of this work. Primary Handling Editors: Jet-Sing Lee and Aldo Isidori.

Reprints and permission information is available at http://www.nature.com/reprints

Publisher's note Springer Nature remains neutral with regard to jurisdictional claims in published maps and institutional affiliations.